ACS APPLIED MATERIALS & INTERFACES
Research Article
www.acsami.org

Growth, Structure, and Thermal Conductivity of Yttria-Stabilized Hafnia Thin Films

C.V. Ramana,*[†] M. Noor-A-Alam,[†] Jamie J. Gengler,[‡,§] and John G. Jones[§]

[†]Department of Mechanical Engineering, University of Texas at El Paso, El Paso, Texas 79968, United States
[‡]Spectral Energies, LLC, 5100 Springfield Street, Suite 301, Dayton, Ohio 45431, United States
[§]Air Force Research Laboratory, Materials and Manufacturing Directorate, Thermal Sciences and Materials Branch, 2941 Hobson Way, Wright-Patterson Air Force Base, Ohio 45433, United States

ABSTRACT: Yttria-stabilized hafnia (YSH) films of 90 nm thickness have been produced using sputter-deposition by varying the growth temperature (T_s) from room-temperature (RT) to 400 °C. The effect of T_s on the structure, morphology, and thermal conductivity of YSH films has been investigated. Structural studies indicate that YSH films crystallize in the cubic phase. The lattice constant decreases from 5.15 to 5.10 Å with increasing T_s. The average grain size (L) increases with increasing T_s; $L-T_s$ relationship indicates the thermally activated process of the crystallization of YSH films. The analyses indicate a critical temperature to promote nanocrystalline, cubic YSH films is 300 °C, which is higher compare to that of pure monoclinic HfO_2 films. Compared to pure nanocrystalline hafnia, the addition of yttria lowers the effective thermal conductivity. The effect of grain size on thermal conductivity is also explored.

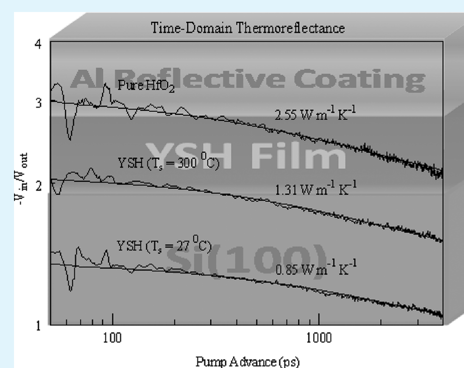

KEYWORDS: *yttria-stabilized hafnia, thin films, growth, structure, thermal conductivity, time-domain thermoreflectance*

1. INTRODUCTION

Hafnium oxide (HfO_2) is a high-temperature refractory material with excellent physical, electronic, and chemical properties.[1−10] The outstanding chemical stability, electrical and mechanical properties, high dielectric constant (high-k), and wide band gap of HfO_2 makes it suitable for several industrial applications in the field of electronics, magneto-electronics, structural ceramics, and optoelectronics.[1−6] HfO_2 has been identified as one of the most promising dielectrics for the nanoelectronics industry to replace SiO_2.[6]

HfO_2 exhibits various polymorphs; monoclinic, tetragonal, and cubic. The stable structure of HfO_2 is monoclinic under normal conditions of temperature and pressure.[9,10] It transforms into the tetragonal form when heated to temperatures higher than 1700 °C.[9,10] Further transformation into the cubic polymorphic form having the fluorite structure takes place at 2700 °C. Similar to zirconia (ZrO_2), doping a small amount of yttria (Y_2O_3) stabilizes the HfO_2 cubic phase (Fm3m space group), which exists at high temperatures.[11−18] The overall cubic symmetry of HfO_2 is preserved down to room temperature in yttria-stabilized hafnia (YSH), which belongs to the group of fluorite-structured (CaF_2) oxygen superionic conductors.[11] Interest in yttria-stabilized zirconia and hafnia materials is generated because of a wide variety of their high temperature applications involving solid oxide fuel cells, oxygen sensors, etc.[17,18] In addition, YSH is used as thermal barrier coatings to protect metallic components such as combustion cans, blades, vanes, etc., of the hot sections of aerospace and land-based gas turbines against high-temperature environments.

Cubic hafnia stabilized at room temperature has been shown to exhibit an increased dielectric constant compared to that in the monoclinic phase, the most common form of hafnia.[13−16] Stabilized cubic hafnia, therefore, provides a platform to explore the fundamental science and future technological applications. However, compared to various potential applications and the structure property relation of yttria-stabilized zirconia (YSZ) studied in the recent past,[17−29] the fundamental microscopic characteristics and thermal conductivity mechanism of YSH materials are not well understood, specifically at reduced dimensions. Although macroscopic studies and some computational work exist, the ultramicrostructure and property relationships in YSH materials are scarce in the literature. Specifically, the focus toward understanding thermal properties of YSH coatings is meager. It is, therefore, of interest to investigate the correlation between microstructure and thermal conductivity in YSH films as a function of growth conditions which is the impetus for the present work. A correlation between the crystal structure, grain size, and thermal conductivity of YSH films made by radio frequency magnetron sputtering is presented and discussed in this paper.

2. EXPERIMENTAL SECTION

A. Fabrication. The yttria-doped hafnia (YSH) coatings were deposited onto silicon (Si) (100) wafers by radio frequency magnetron

Received: September 16, 2011
Accepted: November 14, 2011
Published: December 12, 2011

 © 2011 American Chemical Society

sputtering. All the substrates were thoroughly cleaned and dried with nitrogen before introducing them into the vacuum chamber, which was initially evacuated to a base pressure of ~0.21 mPa. YSH target (5 cm diameter, 0.32 cm thick) (Plasmaterials Inc.) was used for sputtering. The composition of yttria in YSH was maintained at 7.5 mol % (7.5 YSH). The YSH target was placed on a sputter gun, which was correspondingly placed at a distance of 8 cm from the substrate. A sputtering power of 30 W was initially applied to the target while introducing high purity argon (Ar) into the chamber causing plasma ignition. Once ignited, the power was increased to 100W to deposit the films. The flow of the Ar was controlled using an MKS mass flow meter. Before each deposition, the YSH-target was presputtered for 10 min using Ar, keeping the shutter above the gun closed. Deposition was made to obtain a ~90 nm thick coating. The samples were deposited at different temperatures (T_s) varying from room temperature (RT) to 400 °C. The substrates were heated by halogen lamps and the desired temperature was controlled by an Athena X25 controller.

B. Characterization. The grown YSH coatings were characterized by performing structure, morphology and thermal conductivity measurements. To avoid interference by the substrate and obtain diffraction pattern of the coatings, we performed grazing incidence X-ray diffraction (GIXRD) on the YSH coatings. GIXRD measurements were performed using a Bruker D8 Advance X-ray diffractometer. All the measurements were made ex-situ as a function of T_s. GIXRD patterns were recorded using Cu Kα radiation (λ = 1.54056 Å) at RT. A high voltage of 40 kV was used to generate the X-rays. The GIXRD patterns were recorded employing the X-ray beam fixed at a grazing incidence of 1°. The scanning was performed in a 2θ range of 15−70° using the "detector scan" mode, where the detector was independently moved in the plane of incidence to collect the diffraction pattern. The step size and the scan speed were 0.05° (2θ) and 5°/min, respectively. For these set of conditions, the X-ray beam passes sufficiently long distance through the coating along to provide the observed diffraction patterns.

Surface imaging analysis was performed using a high-performance and ultra-high-resolution scanning electron microscope (Hitachi S-4800). The secondary electron imaging was performed on YSH films grown on Si wafers using carbon paste at the ends to avoid charging problems. The grain detection, size-analysis, and statistical analysis were performed using the software provided with the SEM.

Thermal conductivity measurements were performed with a two-color time-domain thermoreflectance (TDTR) lab. This experiment is a modified version of a previously reported system,[30] and details of the modifications only will be given here. The output of a mode-locked Ti:sapphire laser (λ = 787 nm) is split into a pump and a probe beam. The pump beam is sent first through a pulse compressor (for correction of pulse-stretching effects) and then through an electro-optic modulator (EOM), which imposes a square-wave pulse train with a frequency of 9.8 MHz. The pump beam is then aligned along a mechanical translation stage to alter systematically the timing between the pump and the probe pulses. The probe beam is sent through an optical parametric oscillator for wavelength modification (λ = 700 nm). Both pump and probe beams also have half-waveplate/polarizer combinations for arbitrarily controlling the beam intensity. Both beams are then focused to a spot size of ~50 μm diameter at a 45° angle to the sample. The reflected probe beam is spatially filtered, recollimated, and sent through a 750 nm short-pass optical filter to reject scattered pump-beam light (polarization filtering is not required). Finally, the probe beam is passed through a neutral-density filter (optical density = 1.0) and focused onto a silicon (Si) photodiode detector. The output of the detector is sent to the input of a dual-phase, radio frequency (RF) lock-in amplifier that has its reference channel connected to the same electronic signal that drives the EOM. The scans and data acquisition are computer controlled by means of a homemade LabVIEW program.

The YSH samples were coated with an ~80−100 nm thick layer of sputtered aluminum (Al) to produce a high reflectivity surface, which is a standard procedure for the TDTR technique. The layer sequence of the Si substrate substrate, YSH film, and Al over layer reflective coating is schematically represented in Figure 1. Sputtering was conducted in a vacuum chamber with a base pressure of <1 × 10^{-7} Pa to obtain a high purity Al film. An unbalanced magnetron fitted with a 5 cm diameter, >99.99% pure Al target was operated with a power density of ~50 W in a 0.2 Pa Ar background. Samples were insulated from ground during Al deposition and were not actively heated or cooled. In order to compare and contrast thermal conductivity of nanocrystalline, cubic YSH samples, a pure, nanocrystalline, monoclininc HfO_2 sample with a comparable grain size was also examined following the same procedure and TDTR method.

Figure 1. Schematic diagram of the layer sequence grown for thermal conductivity measurements. The Si substrate, YSH film, and Al top layer reflecting coating are as shown.

3. RESULTS AND DISCUSSION

A. Crystal Structure. The XRD patterns of YSH films are shown in Figure 2 as a function of T_s. The XRD curves of YSH films exhibit the peaks corresponding to cubic structure of

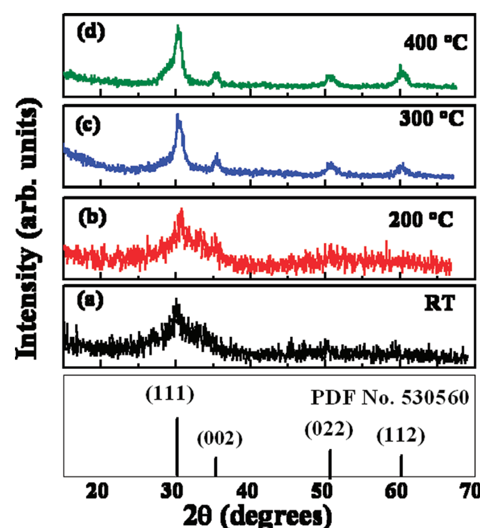

Figure 2. XRD patterns of YSH coatings grown at various substrate temperatures. YSH coatings grown at various substrate temperature exhibits the cubic phase as indexed. The PDF of cubic hafnia is presented for comparing the data of YSH coatings obtained in the present work.

HfO_2. It is evident (Figure 2) that the peak at ~30.28° which corresponds to diffraction from (111) planes is rather broad for films grown at T_s = RT-200 °C indicating the presence of nanocrystalline particles embedded in an amorphous matrix. The intensity and the width of the (111) peak increases with increasing T_s. This is indicative of an increase in the average crystallite-size and preferred orientation of the film along (111). The lattice parameter determined from XRD curves exhibit a decreasing trend from 5.15 to 5.10 (±0.001) Å with T_s (RT to 400 °C). Figure 3 shows the variation of lattice parameter with T_s. We attribute this decrease in lattice parameter to the changes in lattice-strain and crystallite size in nanocrystalline YSH films with increasing T_s. The lattice constant obtained for YSH coatings is larger compared to that of pure HfO_2 (5.09 Å).[31] This lattice expansion in YSH compared to pure HfO_2 is caused by the addition of 7.5% Y_2O_3 and can be understood as follows. The ionic radii of Y^{3+}(0.96 Å) is larger than that of Hf^{4+} which introduces lattice distortion and enforce the elongation of bond with oxygen in close proximity. Monoclinic and tetragonal phases consist of several shorter Hf−O bond lengths (2.0−2.1 Å) compared to cubic HfO_2 (2.37 Å).[31] As a consequence, the strain energy because of the size mismatch becomes significant in monoclinic and tetragonal phases. On the other hand, the distortion is quite less in cubic phase with the oversized Y^{3+} doping, which makes cubic HfO_2 stable even at low temperature. Furthermore, the structural relaxation plays another role in the stabilization of cubic phase of HfO_2 by Y_2O_3 dopant.[32]

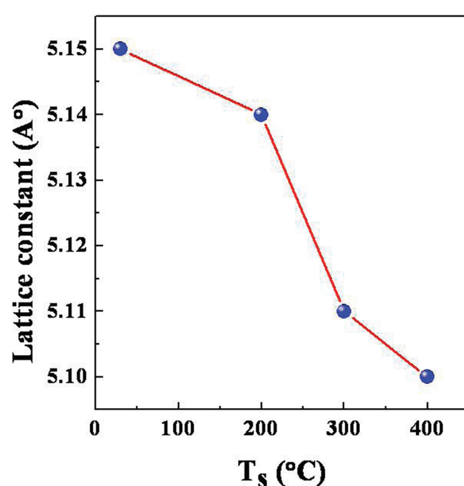

Figure 3. Variation of lattice constant as a function of T_s for YSH coatings. Line provides a guide to the eye.

B. Surface Morphology. SEM images of YSH films as a function of T_s are shown in Figure 4. The effect of T_s on the surface morphology of YSH films is remarkable. The small, dense particles can be noticed in SEM images. The fine microstructure and uniform distribution characteristics of the particles are evident in the micrographs (Figure 4). The average size increases with increasing T_s as seen in the micrographs. Based on the observations of XRD, SEM and data analyses, the effect of temperature on the microstructure evolution of YSH films can be explained as follows. If temperature is low such that the period of the atomic jump process of adatoms on the substrate surface is very large, the condensed species may stay stuck to the regions where they are landing, thus leading to amorphous YSH films. The adatom mobility on the surface increases with increasing T_s.[32,33] The SEM data coupled with appearance of diffraction peaks in XRD clearly indicate that 300 °C is the critical temperature to promote the growth of nanocrystalline YSH films. The average grain size values for YSH films grown at 300 and 400 °C were 21 and 25 nm, respectively. The temperature observed for crystallization of YSH films is higher compared to the critical temperature (200 °C) required to promote the growth of nanocrystalline, monoclinic pure hafnia films using sputter-deposition as reported elsewhere.[34] However, YSH films grown in this work employing YSH target crystallize at lower temperatures without needing postdeposition annealing at higher temperatures and under controlled environment as encountered in films grown using cosputtering of Y and Hf targets.[13] The surface morphology of pure, monoclinic hafnia sample is presented in Figure 4 (image C) for comparison. The average grain size of monoclinic HfO_2 films is 23 nm.

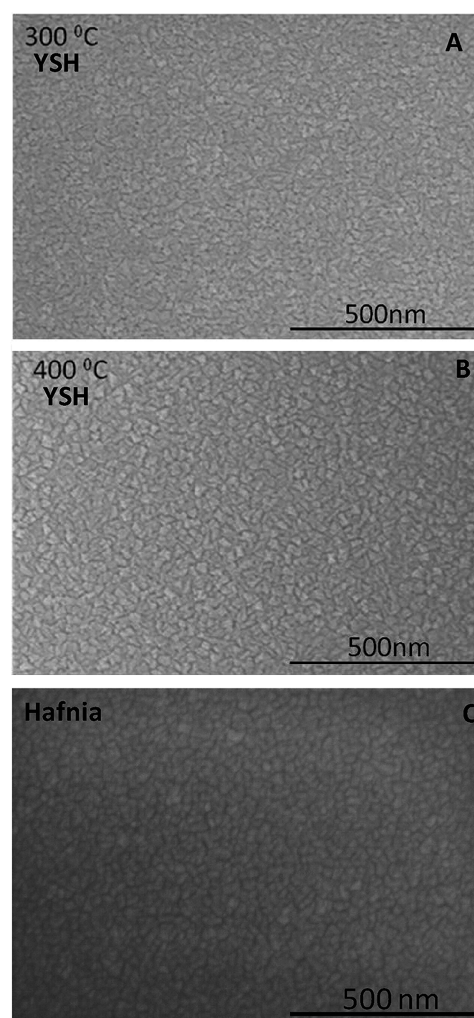

Figure 4. SEM images of nanocrystalline, cubic YSH coatings grown at 300 °C (image A) and 400 °C (image B). Surface morphology of pure, monoclininc hafnia with comparable grain size employed for thermal conductivity measurements is also shown for comparison.

C. Thermal Properties. Analysis of the data for extraction of thermal conductivities was accomplished with a frequency-domain model[35] in which the ratio of the in-phase and out-of-phase lock-in amplifier signals is calculated as a function of time

dx.doi.org/10.1021/am2012596 | ACS Appl. Mater. Interfaces 2012, 4, 200−204

$$-\frac{V_{in}}{V_{out}} = \left(\sum_{-m}^{m} (\Delta T(m/\tau + f) + \Delta T(m/\tau - f)) \exp(i2\pi mt/\tau) \right) / \left(i \sum_{-m}^{m} (\Delta T(m/\tau + f) - \Delta T(m/\tau - f)) \exp(i2\pi mt/\tau) \right) \quad (1)$$

Here m is an integer denoting summation over pump pulses, τ the time between unmodulated laser pulses (12.5 ns), f the modulation frequency (9.8 MHz), and t the time delay between pump and probe pulses. The function ΔT is calculated with the Feldman matrix algorithm as explained in reference 35 (eq 1 is also multiplied by a phase shift of $e^{i2\pi ft}$). The function ΔT is the calculated temperature excursion at the surface of the sample

$$\Delta T = 2\pi A \int_0^{\infty} G(k) e^{-(\pi kw)^2} k dk \quad (2)$$

In eq 2, A is the absorbed laser fluence, w is the spot radii of the focused pump and probe beams (assuming equal Gaussian profiles), and k is an inverse space variable. For layered structures, the function $G(k)$ is calculated with the Feldman matrix algorithm as fully explained in ref 35. Data for pump advance times earlier than t = 100 ps were not taken into account because electron−phonon coupling was not equilibrated, which allows the Al film to reach a uniform temperature. Picosecond acoustics also perturb this regime (which facilitates direct measurements of the Al thickness). For the model, a five-layer system was used comprised of two layers for the Al film (as explained in reference 35), an interfacial conductance, 90 nm for the sample layer, and a semi-infinite silicon substrate. This five-layer system was used since the sample thicknesses were comparable to the thermal penetration depth of the experiment $(D/2\pi f)^{1/2} \approx 100$ nm. Here D is the thermal diffusivity of the sample layer and f is the TDTR modulation frequency. When the sample thickness is comparable to the thermal penetration depth, the TDTR experiment will be sensitive to the nature of the substrate. Therefore, it was deemed necessary to explicitly include the 90 nm sample thickness when modeling the TDTR data. In modeling the data, a volumetric heat capacity of 2.73 J cm^{-3} K^{-1} was used.[36,37] For the samples studied, TDTR data were acquired from five locations on each sample surface. The scans were individually modeled, and an average thermal conductivity ± standard deviation value was calculated for each sample.

Illustrated in Figure 5 are representative raw data and models for the pure and YSH samples that were measured with TDTR. The thermal conductivity result for the pure hafnia sample of nanocrystalline, monoclinic structure was 2.57 ± 0.12 W m^{-1} K^{-1}, which is slightly higher than the values reported for the similar materials of polycrystalline yttria-stabilized zirconia (YSZ)[38] and YSH[36] (~2.3 W m^{-1} K^{-1}). Addition of yttria to hafnia, as seen in the other 3 samples studied with TDTR, resulted in significant decreases to the effective thermal conductivity. The YSH sample with T_s = 27 °C had a thermal conductivity result of 0.87 ± 0.03 W m^{-1} K^{-1}. This large

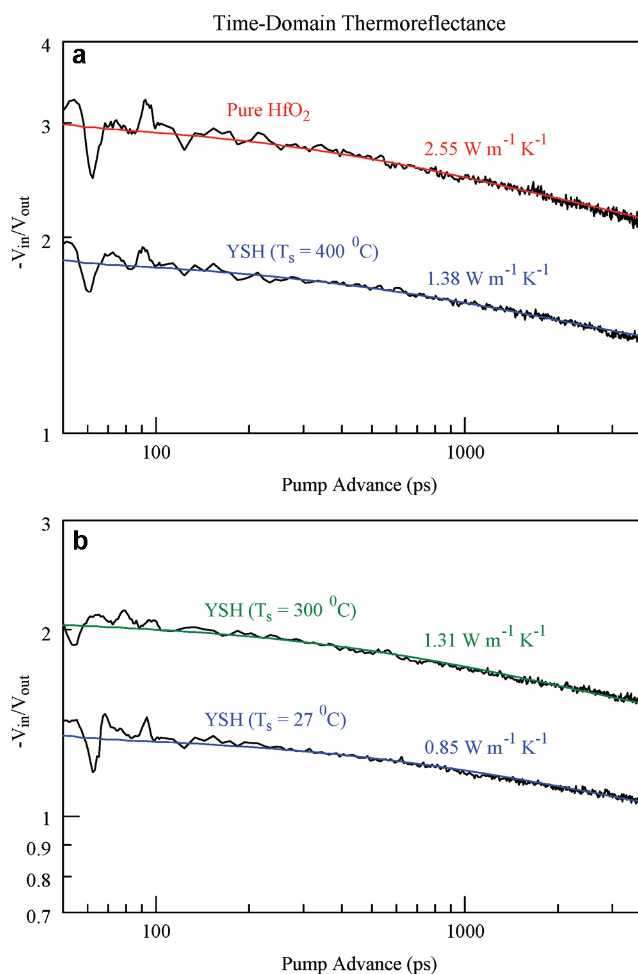

Figure 5. Individual scans of TDTR data and models for (a) pure hafnia and YSH films with T_s = 400 °C, and (b) YSH films grown at 300 and 27 °C.

decrease can primarily be attributed to an amorphous structure, which is exemplified in the XRD data of Figure 2a. Amorphous materials are known to have lower thermal conductivity than their crystalline counterparts. This can be attributed to hindered phonon transport in disordered materials arising from random, noncentral distortions of the lattice.[39] A minimum thermal conductivity can be achieved when the phonon mean free path equals the phonon wavelength (governed by the speed of sound in the solid).[40] An additional reason for YSH materials exhibiting lower thermal conductivity than pure hafnia is the introduction of oxygen vacancies.[36] These are structural vacancies in the hafnia monoclinic crystals due to charge compensation of Y^{3+} ions substituting for Hf^{4+} ions. As a result, phonon scattering from the vacancies decreases effective thermal transport.

For the samples of YSH with T_s = 300 and 400 °C, the thermal conductivities were 1.31 ± 0.03 W m^{-1} K^{-1} and 1.35 ± 0.04 W m^{-1} K^{-1}, respectively. The increase in these values compared to the amorphous structure can be attributed to crystalline formation, evidenced in the XRD data of Figure 2c,d. The slight increase in thermal conductivity between the YSH samples of T_s = 300 and 400 °C can also be related to the slight increase in grain size (from 21 nm to 25 nm). This trend of increasing thermal conductivity with increasing grain size has been found for YSZ samples[38] and has been rationalized as

decreased grain boundaries in larger grain materials can decrease phonon scattering. However, it should be noted that the thermal conductivity of YSH samples are low compared to that of pure, monoclinic HfO_2 samples with comparable grain size (23 nm). The relationship between grain size and thermal conductivity bridges the regimes of amorphous materials (random structure) and crystalline materials (lattice structure). As grains form (crystallize) and coalesce, the material becomes more ordered. The random scattering sites in amorphous materials are replaced by grain boundaries. As the grains become larger, the number of grain−grain interfaces becomes smaller and hence phonon interfacial scattering becomes reduced, thereby increasing the effective thermal conductivity of the material.

4. CONCLUSIONS

Yttria-stabilized films of 90 nm thick were fabricated using sputter-deposition at variable growth temperatures ranging from room-temperature to 400 °C. The structural and thermal properties of the YSH films were investigated. The effect of growth temperature is significant on the structure and thermal conductivity of the YSH films. X-ray diffraction and scanning electron microscopy analyses indicate that YSH films are amorphous below 300 °C, at which point an amorphous-to-crystalline transformation occurs. YSH films crystallize in the cubic phase. The critical temperature to promote nanocrystalline, cubic YSH film growth is higher compared to that of pure monoclinic HfO_2 films. Yttria-stabilization of hafnia films in cubic phase significantly lowers the effective thermal conductivity compared to pure monoclinic hafnia films. The thermal conductivity of amorphous YSH films is 0.87 ± 0.03 $Wm^{1-}K^{-1}$ and that of nanocrystalline cubic YSH films is 1.31 ± 0.03 $Wm^{1-}K^{-1}$. The effective reduction in thermal conductivity of YSH films is promising to utilize these materials in high-temperature protective applications.

■ AUTHOR INFORMATION

Corresponding Author

*E-mail: rvchintalapalle@utep.edu.

■ ACKNOWLEDGMENTS

This material is based on the work supported by the Department of Energy (DOE) under Award DE-FE0000765. The authors at the University of Texas at El Paso acknowledge with pleasure the support from DOE. The thermal conductivity measurement system acquisition and operation at the Air Force Research Laboratory was supported under Contract FA8650-07-D-5800.

■ REFERENCES

(1) Ramo, D. M.; Shluger, A. L.; Gavarton, J. L.; Bersuker, G. *Phys. Rev. Lett.* **2007**, *99*, 155504.

(2) Hong, N. H.; Poirot, N.; Sakai., J. *Appl. Phys. Lett.* **2006**, *89*, 042503.

(3) Miyata, N.; Yasuda, T.; Abe, Y. *J. Appl. Phys.* **2010**, *107*, 103536.

(4) Jiang, K.; Anderson, J. T.; Hoshino, k.; Li, d.; Wager, J. F.; Keszler, D. A. *Chem. Mater.* **2011**, *23*, 945.

(5) Armelao, L.; Bertagnolli, H.; Bleiner, D.; Groenewolt, M.; Gross, S. *Adv. Funct. Mater.* **2007**, *17*, 1671.

(6) Robertson, J. *Rep. Prog. Phys.* **2006**, *80*, 1249.

(7) Kingdom, A. I.; Maria, J. P.; Streiffer, S. K. *Nature* **2000**, *406*, 1032.

(8) Wilk, G. D.; Wallace, R. M.; Anthony, J. M. *J. Appl. Phys.* **2001**, *89*, 5243.

(9) Ferrari, S.; Modreanu, M.; Scarel, G.; Fancinelli, M. *Thin Solid Films* **2004**, *450*, 124.

(10) Villanueva, M. I.; Luyer, C. L.; Parola, S.; Marty, O.; Mugnier, J. *Rev. Adv. Mater. Sci.* **2003**, *5*, 296.

(11) Tang, J.; Zhang, F.; Zoogman, P.; Fabbri, J.; Chan, S.-W.; Zhu, Y.; Brus, L. E.; Steigerwald, M. L. *Adv. Funct. Mater.* **2005**, *15*, 1595.

(12) Nishide, T.; Honda, S.; Matsuura, M.; Ito, Y.; Takase, T. *Jpn. J. Appl. Phys.* **2000**, *39*, L237.

(13) Kita, K.; Kyuno, K.; Toriumi, T. *App. Phys. Lett.* **2005**, *86*, 102906.

(14) Niinistö, J.; Kukli, K.; Sajavaara, T.; Ritala, M.; Leskelä, M.; Oberbeck, L.; Sundqvist, J.; Schröder, U. *Electrochem. Solid-State Lett.* **2009**, *12*, G1.

(15) Rauwel, E.; Dubourdieu, C.; Holländer, B.; Rochat, N.; Rossell, M. D.; Van Tendeloo, G.; Pelissier, B. *Appl. Phys. Lett.* **2006**, *89*, 012902.

(16) Yang, Z. K.; Lee, W. C.; Lee, Y. J.; Chang, P.; Huang, M. L.; Hong, M.; Yu, K. L.; Tang, M,T.; Lin, B. H.; Hsu, C. H.; Kwo, J. *App. Phys. Lett.* **2007**, *91*, 202909.

(17) Kadlec, F.; Simon, P. *Mater. Sci. Eng., B* **2000**, *72*, 56.

(18) Campo, L.d.; Meneses, D. D. S.; Blin, A.; Rousseau, B.; Veron, E. *J. Am. Ceram. Soc.* **2011**, *1*, 6.

(19) Bazin, N.; Andrew, J. E.; McInnes, H. A. *J Sol−Gel Sci. Technol.* **1998**, *13*, 757.

(20) Zhang, Q. Y.; Li, X. L.; Shen, J.; Wu, G. M.; Wang, J.; Chen, L. Y. *Mater. Lett.* **2000**, *45*, 311.

(21) Tong, L. M. *J. Cryst. Growth* **2000**, *217*, 281.

(22) Rogers, P. H.; Sirinakis, G.; Carpenter, M. A. *J. Phys. Chem. C* **2008**, *112*, 6749.

(23) Sirinakis, G.; Siddique, R.; Manning, I.; Rogers, P. H.; Carpenter, M. A. *J Phys. Chem. B* **2006**, *110*, 13508.

(24) Muratore, C.; Clarke, D. R.; Jones, J. G.; Voevodin, A. A. *Wear* **2008**, *265*, 913.

(25) Glushkova, V. B.; Krzhizhanovskaya, V. A. *Ceram. Int.* **1985**, *11*, 80.

(26) Shim, J. H.; Chao, C.-C.; Huang, H.; Prinz, F. B. *Chem. Mater.* **2007**, *19*, 3850.

(27) Huang, H.; Nakamura, M.; Su, P.; Fasching, R.; Saito, Y.; Prinz, F. B. *J. Electrochem. Soc.* **2007**, *154*, B20.

(28) Xiang, X.; Zu, X. T.; Zhu, S.; Zhang, C. F.; Wang, Z. G.; Wang, L. M.; Ewing, R. C. *Nucl. Instrum. Methods* **2006**, *250*, 382.

(29) Zhu, S.; Zu, X. T.; Wang, L. M.; Ewing, R. C. *Appl. Phys. Lett.* **2002**, *80*, 4327.

(30) Gengler, J. J.; Muratore, C.; Roy, A. K.; Hu, J.; Voevodin, A. A.; Roy, S.; Gord, J. R. *Compos. Sci. Technol.* **2010**, *70*, 2117.

(31) Choong, K. L.; Eunae, C.; Hyo, S. L.; Cheol, S. H.; Seungwu, H. *Phys. Rev. B* **2008**, *78*, 012102.

(32) Kalidindi, N. R.; Manciu, F. S.; Ramana, C. V. *ACS Appl. Mater. Inter.* **2011**, *3*, 863−868.

(33) Mudavakkat, V. H.; Noor-A-Alam, M.; Kamala Bharathi, K.; AlFiafy, S.; Dissanayeke, K.; Kayani, A.; Ramana, C. V. *Thin Solid Films* **2011**, *519*, 7947.

(34) Agguirre, B.; Vemuri, R. S.; Zubia, D.; Shutthanandan, S.; Engelhard, M. H.; Kamala Bharathi, K.; Ramana, C. V. *Appl. Surf. Sci.* **2011**, *257*, 2197.

(35) Cahill, D. G. *Rev. Sci. Instrum.* **2004**, *75*, 5119.

(36) Winter, M. R.; Clarke, D. R. *Acta Mater.* **2006**, *54*, 5051.

(37) Wang, C.; Zinkevich, M; Aldinger, F. *J. Am. Ceram. Soc.* **2006**, *89*, 3751.

(38) Soyez, G.; Eastman, J. A.; Thompson, L. J.; Bai, G.-R.; Baldo, P. M.; McCormick, A. W.; DiMelfi, R. J.; Elmustafa, A. A.; Tambwe, M. F.; Stone, D. S. *Appl. Phys. Lett.* **2000**, *77*, 1155.

(39) Cahill, D. G.; Watson, S. K.; Pohl, R. O. *Phys. Rev. B* **1992**, *46*, 6131.

(40) Cahill, D. G.; Pohl, R. O. *Phys. Rev. B* **1987**, *35*, 4067.